remote sensing

MDPI

Article

ES-L2-VGG16 Model for Artificial Intelligent Identification of Ice Avalanche Hidden Danger

Daojing Guo [1,2], Minggao Tang [1,2,*], Qiang Xu [1,2], Guangjian Wu [3], Guang Li [1,2], Wei Yang [3], Zhihang Long [1,2], Huanle Zhao [1,2] and Yu Ren [1,2]

[1] State Key Laboratory of Geohazard Prevention and Geoenvironment Protection, Chengdu University of Technology, Chengdu 610059, China; gdj@stu.cdut.edu.cn (D.G.); xq@cdut.edu.cn (Q.X.); liguang0320@stu.cdut.edu.cn (G.L.); longzhixing@stu.cdut.edu.cn (Z.L.); 2020010067@stu.cdut.edu.cn (H.Z.); ry@stu.cdut.edu.cn (Y.R.)
[2] College of Environment and Civil Engineering, Chengdu University of Technology, Chengdu 610059, China
[3] Institute of Tibetan Plateau Research, Chinese Academy of Sciences, Beijing 100101, China; wugj@itpcas.ac.cn (G.W.); yangww@itpcas.ac.cn (W.Y.)
* Correspondence: tmg@cdut.edu.cn

Abstract: Ice avalanche (IA) has a strong concealment and sudden characteristics, which can cause severe disasters. The early identification of IA hidden danger is of great value for disaster prevention and mitigation. However, it is very difficult, and there is poor efficiency in identifying it by site investigation or manual remote sensing. So, an artificial intelligence method for the identification of IA hidden dangers using a deep learning model has been proposed, with the glacier area of the Yarlung Tsangpo River Gorge in Nyingchi selected for identification and validation. First, through engineering geological investigations, three key identification indices for IA hidden dangers are established, glacier source, slope angle, and cracks. Sentinel-2A satellite data, Google Earth, and ArcGIS are used to extract these indices and construct a feature dataset for the study and validation area. Next, key performance metrics, such as training accuracy, validation accuracy, test accuracy, and loss rates, are compared to assess the performance of the ResNet50 (Residual Neural Network 50) and VGG16 (Visual Geometry Group 16) models. The VGG16 model (96.09% training accuracy) is selected and optimized, using Early Stopping (ES) to prevent overfitting and L2 regularization techniques (L2) to add weight penalties, which constrained model complexity and enhanced simplicity and generalization, ultimately developing the ES-L2-VGG16 (Early Stopping—L2 Norm Regularization Techniques—Visual Geometry Group 16) model (98.61% training accuracy). Lastly, during the validation phase, the model is applied to the Yarlung Tsangpo River Gorge glacier area on the Tibetan Plateau (TP), identifying a total of 100 IA hidden danger areas, with average slopes ranging between 34° and 48°. The ES-L2-VGG16 model achieves an accuracy of 96% in identifying these hidden danger areas, ensuring the precise identification of IA dangers. This study offers a new intelligent technical method for identifying IA hidden danger, with clear advantages and promising application prospects.

Keywords: ice avalanche; hidden danger; early identification; artificial intelligent; ES-L2-VGG16 model; deep learning; Tibetan Plateau

Citation: Guo, D.; Tang, M.; Xu, Q.; Wu, G.; Li, G.; Yang, W.; Long, Z.; Zhao, H.; Ren, Y. ES-L2-VGG16 Model for Artificial Intelligent Identification of Ice Avalanche Hidden Danger. *Remote Sens.* **2024**, *16*, 4041. https://doi.org/10.3390/rs16214041

Academic Editor: Xianwei Wang

Received: 26 August 2024
Revised: 25 October 2024
Accepted: 27 October 2024
Published: 30 October 2024

1. Introduction

As global climate change intensifies, extreme weather events are becoming more frequent and severe, making ice avalanches (IAs) a common natural disaster in High Mountain Asia (HMA). IAs occur when glacier ice collapses along shear planes or weak surfaces on steep slopes, forming debris flows and triggering secondary disasters [1]. With the increasing frequency and scale of IAs, IA hidden danger, which refers to the likelihood of an IA occurring due to glacier instability, steep terrain, crack development, and external environmental factors, poses an increasingly severe threat to ecosystems and human safety [2,3]. On the Tibetan Plateau (TP) and other glacier-dense regions, over

40,963 glaciers cover about 45,000 km^2, significantly affecting local life, property, and the environment [4,5]. Herein, the early identification of IA hidden dangers is crucial for prevention and danger mitigation.

At present, the traditional methods of identifying IA hidden dangers are mainly site geological survey, remote sensing interpretation, and historical data evaluation [6]. LaChapelle [7] used artificial control and empirical judgment for avalanche identification, but the accuracy remains insufficient for more precise predictions. Tang et al. [2] identified the hidden dangers of ice avalanche on the Tibetan Plateau using an interactive remote sensing interpretation manually and via computer. Due to the high altitude and the harsh environment of the IA area, it is very difficult and inefficient to identify that by site investigation or manual remote sensing.

In recent years, due to the outstanding performance of image processing and pattern recognition, deep learning technologies have shown great potential in the intelligent recognition of geohazards. Numerous scholars have explored applying deep learning methods to identify and predict geohazards [8]. These efforts improve recognition accuracy and automation, reducing experimental expenses and human bias. For example, Choubin et al. [9,10] combined glacier-monitoring data with terrain features and used deep learning technology to predict the possibility and danger levels of avalanches, thus demonstrating the application of deep learning in IA hidden danger identification. As interdisciplinary research progresses, the demand for deep learning in image recognition and classification is increasing in geological engineering [11]. Although some traditional machine learning methods like Support Vector Machines (SVM), Artificial Neural Networks (ANN), and Random Forests (RF) perform well on simple classification problems [12–14], their efficiency and accuracy can be limited in scenarios involving complex image datasets and high-level abstract feature extraction. Therefore, as part of deep learning, Convolutional Neural Networks (CNN) have demonstrated a superior capability in image recognition.

CNN effectively captures and recognizes complex image patterns by learning hierarchical feature representations of images. Lin et al. [15] and Wang et al. [16] studied high-resolution geological maps, geological structures, and landslide susceptibility, successfully achieving identification, prediction, and categorization. However, traditional CNN models, often using large convolutional kernels, face challenges such as low computational efficiency and the need for extensive network parameters. To enhance the accuracy of network training, researchers have begun exploring deeper network architectures to extract features more effectively. Advanced models such as the Visual Geometry Group 16 (VGG16) and Residual Neural Network 50 (ResNet50) have emerged to improve performance by deepening the network structure. These models provide new technical solutions for the intelligent early warning of geohazards. However, directly applying existing deep learning models like VGG16 or ResNet50 to identify the hidden danger of IA faces challenges such as model overfitting, low training efficiency, and insufficient generalization ability. These issues require further optimization.

Identifying IA hidden danger is challenging, and the efficiency of current optical interpretation methods needs improvement. Herein, we use advanced remote sensing technology and Geographic Information Systems (GIS) to analyze and identify the hidden danger points of IAs on the TP. After evaluating the performance of different deep learning models, the optimized Early Stopping—L2 Norm Regularization—Visual Geometry Group 16 (ES-L2-VGG16) model is developed to enhance accuracy and efficiency in identifying IA hidden dangers. The core purpose is to explore the application of deep learning technology in the intelligent identification of hidden danger of IA. At the same time, the effectiveness and reliability of the model are verified through real-world cases. This promotes the widespread application of deep learning models in natural disaster prediction.

2. Geological Background

Due to unique geological and topographic conditions, coupled with global warming, the TP has become a region prone to frequent IA events. Covering approximately 2.5 million square kilometers (Figure 1), the TP is the largest plateau in western China, featuring a complex terrain with plateaus, mountains, and basins at altitudes exceeding 3000 m. It is one of the world's largest glacier concentration areas, formed by the collision between the Indian and Eurasian plates, and contains multiple geological tectonic units [17]. These tectonic activities have caused significant terrain fluctuations and height instability, contributing to the occurrence of IAs. According to Tang et al. [18], 40,269 glaciers on the TP were identified using remote sensing techniques combined with human–machine interaction, resulting in a database of 581 IA hidden danger points (Figure 1).

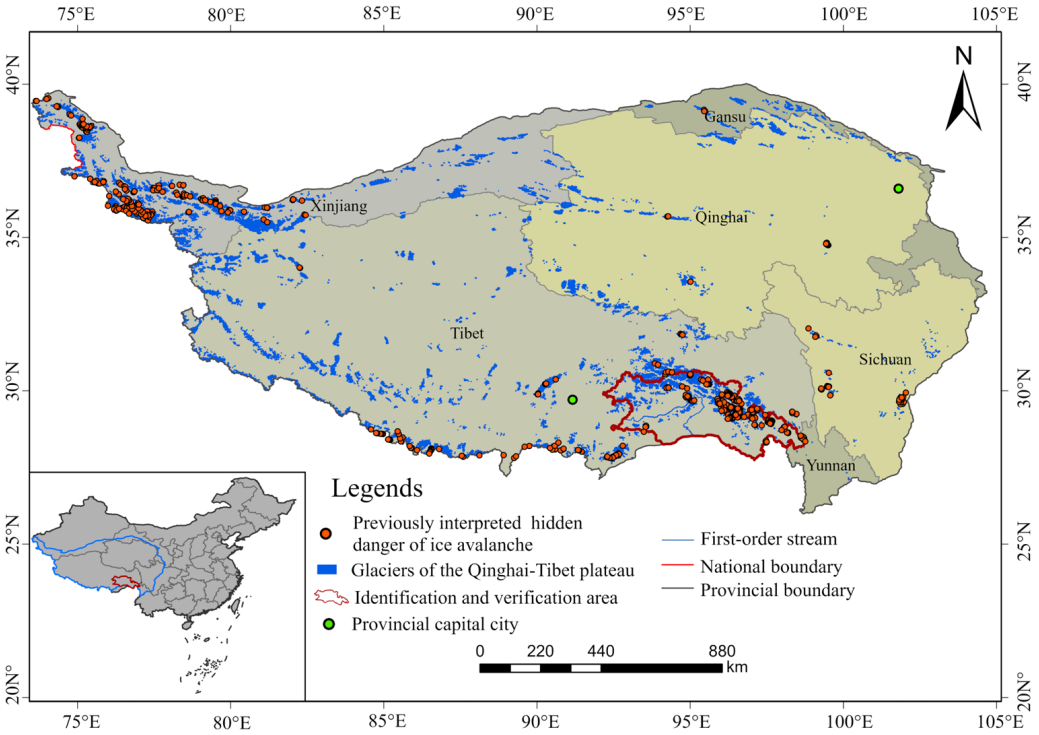

Figure 1. Study and validation area. (the dataset was sourced from the National Earth System Science Data Center (http://www.geodata.cn, accessed on 1 May 2024), and the Second Glacier Inventory of China (V1.0) and processed using ArcGIS software 3.0.1).

In addition, the glaciers are widely distributed in the Yarlung Tsangpo River Basin in southeastern TP, particularly in the Nyingchi region, which is part of the eastern extension of the Himalayan orogenic belt [19]. The terrain is complex and steep, characterized by deep valleys and large slopes [20]. Due to the collision between the Indian and Eurasian plates, the rocks in this region have undergone intense metamorphism, resulting in complex structural geomorphology, including multiple faults and uplifted areas. The region is rich in glacier resources, and the dynamic changes in glaciers directly impact the occurrence of IAs. Glaciers are widely covered, and their movement and changes are critical factors in IA occurrence. In particular, glacier cracks and slope changes significantly impact glacial stability. Increases in glacier cracks and slope steepness may weaken the ice structure, thus promoting IA occurrences.

Therefore, the Yarlung Tsangpo River Gorge in Nyingchi was selected as the core area for identification and validation (Figures 1 and 2). The validation area refers to this glacier-rich region, where a trained model was used to evaluate the hidden danger of IAs, and the model's accuracy is validated through observational data. The complex topography

and dynamic glacial changes in this region make it an ideal area for testing and refining the model's ability to identify IA hidden dangers.

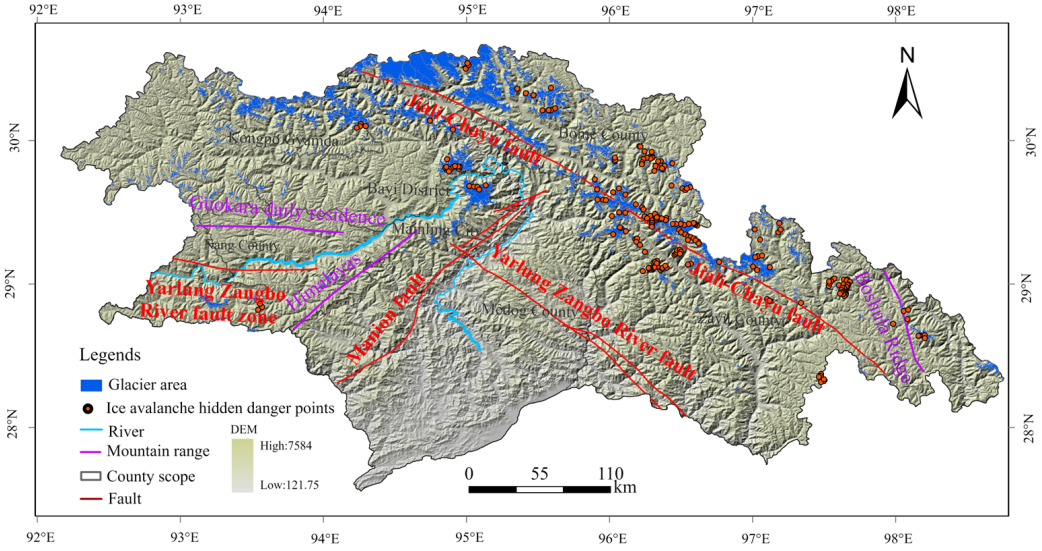

Figure 2. Terrain and geomorphology of verification area. (The DEM data (5 m resolution) was sourced from the Shuttle Radar Topography Mission (SRTM) (http://earthexplorer.usgs.gov/, accessed on 20 May 2024) and processed using ArcGIS software 3.0.1).

In addition, through data collection and field survey, this paper summarizes the historical events of IA in the Yarlung Tsangpo River basin in Linzhi City since the 20th century (Table 1). In the 1980s, the number of IAs showed an increasing trend. Since the turn of the 21st century, the number of IAs in the Yarlung Tsangpo River basin of Linzhi City has exceeded 10 [3]. Among them, the most typical and representative case is the Sedongpu Valley IA.

Table 1. IAs statistics in Linzhi City, China since the 20th century.

No	Name	Longitude/Latitude	Altitude/m	Date	Location	Reference
1	Rumu Lake Basin IA	29.28°N, 96.85°E	4027	1931/7/22 1950/8/15	Bomi	[21]
2	Zelongnong IA	29.75°N, 95.02°E	3650	1968/9/02 1984/4/13	Milin	[22,23]
3	Guxiang Gully IA	29.59°N, 95.29°E	4050	1953/9/29	Bomi	[24]
4	Damenlake Co IA	29.87°N, 93.04°E	5210	1964/9/26 1983/7/29	Gongbujiangda	[25,26]
5	Peilong Gully IA	30.09°N, 94.90°E	4137	1984/8/23 1985/6/20	Nyingchi	[25]
6	Guangxie Co IA	29.46°N, 96.50°E	3816	1988/7/15	Bomi	[27]
7	Yigong Ice-rock Avalanche	30.20°N, 94.97°E	5520	2000/4/9	Bomi	[28]
8	Oguchongguo Co IA	29.63°N, 93.54°E	4680	2003–2004 2007/9/4	Bayi	[29]
9	Tianmo Gully IA	29.96°N, 95.30°E	5560	2010/7/25 2010/9/5	Bomi	[30]
10	Nalongzangbu Gully IA	30.44°N, 94.97°E	4187	2014/6 2017/10/22	Bomi	[29]
11	Sedongpu Valley IA	29.78°N, 94.92°E	6000	2017/12/21 2018/10/17 2018/10/30	Nyingchi	[31]

Geological surveys show that the strata in the Sedongpu area are primarily composed of metamorphic and intrusive rocks, which have undergone multiple folding and faulting events, resulting in complex geological structures. These formations are key factors driving glacier deformation and fracturing. Additionally, the area's unique geographical location and geological conditions make it highly susceptible to surface temperature and precipitation changes, which accelerate glacier crevasse formation and heighten the hidden danger of IAs.

These geological and environmental factors are amplified by the Sedongpu Valley's unique topography. Located on the left bank of the lower Yarlung Tsangpo River, at the terminus of the Eastern Himalayan tectonic knot, the valley has a distinctive funnel-shaped terrain, surrounded by mountains on three sides with steep upper slopes. The terrain not only promotes glacier formation but also, due to its specific slope and orientation, increases the frequency of IAs (Figure 3). The 3D stereo terrain of the Sedongpu Valley is based on DEM elevation data processed on 30 November 2018, highlighting how the abundant glaciers provide ample energy and material for IAs to occur. In the past ten years, there have been several ice avalanche disasters in this region. This paper will take this as a typical case to analyze and extract the following ice avalanche identification indicators.

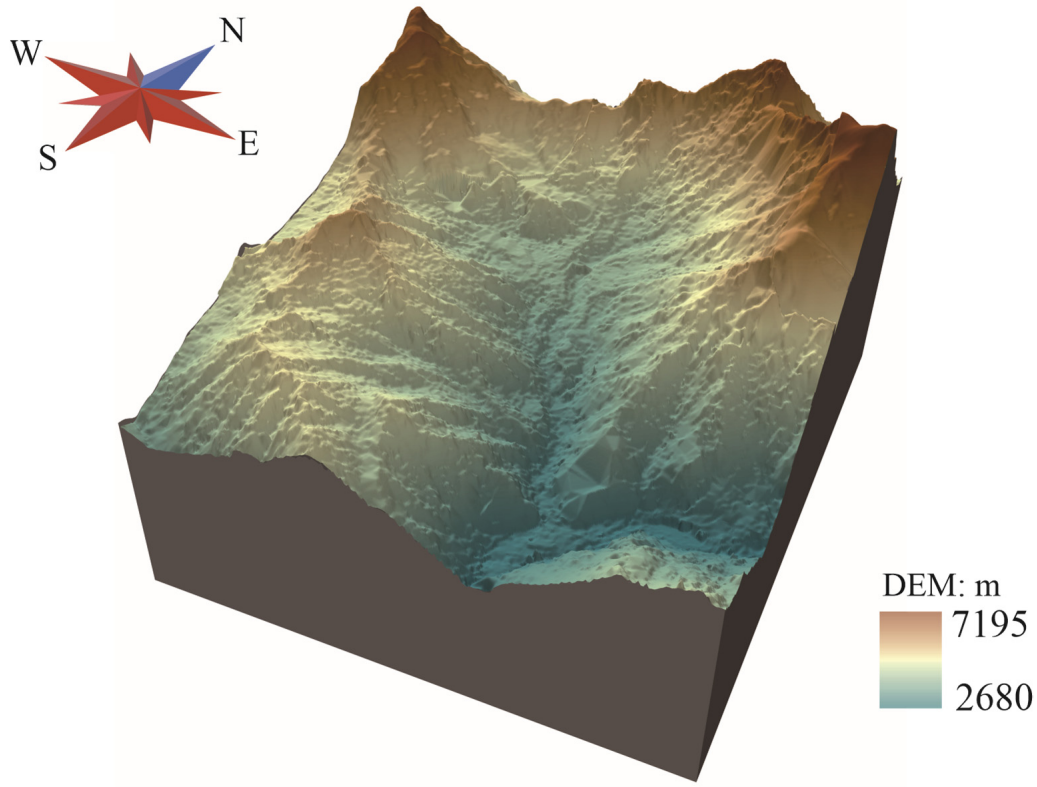

Figure 3. Three-dimensional stereo model of the Sedongpu Valley.

3. Identification Method

Figure 4 summarizes the overall methodology for identifying IA hidden dangers. The methodology is divided into three main sections, data processing and the establishment of identification indicators and danger level classification; model construction, training and optimization; and finally hidden danger identification and validation. A detailed explanation of each step is provided in the following sections.

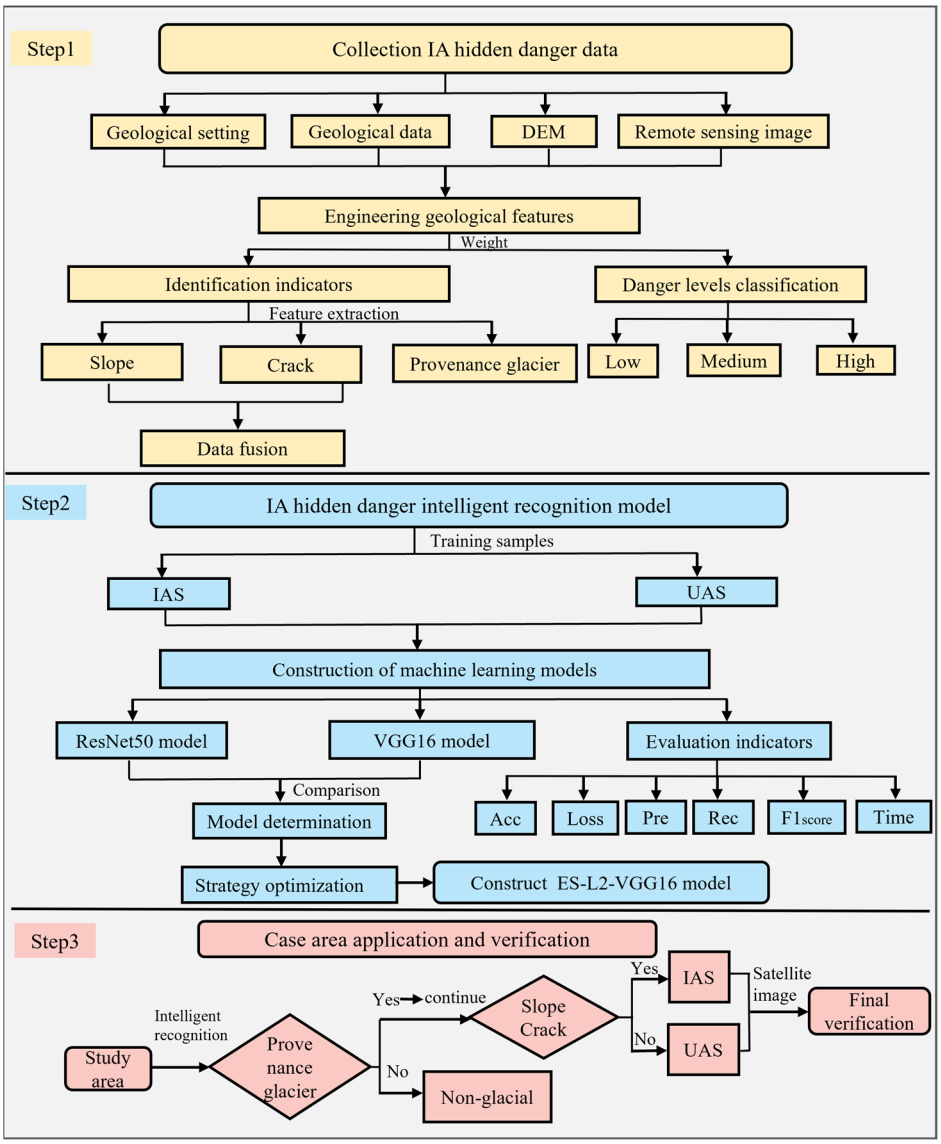

Figure 4. Technical processes and methods of IAs hidden danger intelligent identification.

3.1. Data Collection and Processing

The study area was calibrated using Google Earth pro to ensure the accurate location data for 581 IA hidden danger points on the TP [18]. Additionally, data for 500 uncertain ice avalanches (UAs) hidden danger points were collected for model comparison and training. The primary remote sensing data source was Sentinel-2A satellite imagery, supplemented by a 12.5 m resolution Digital Elevation Model (a) and satellite images with a focus on areas within a 5 km radius around each identified IA hidden danger point.

ArcGIS pro was used to extract key terrain parameters, such as slope, which are crucial for assessing glacier instability. Special attention was given to detecting terrain cracks near the hidden danger points, as these cracks serve as important indicators for identifying IAs. Python scripts were employed to automate the crack detection process and extract relevant features from the images. To minimize interference from cloud cover and snow, images taken during spring and autumn were selected, ensuring high clarity and minimal obstruction.

By integrating remote sensing data with GIS, terrain features were accurately extracted and prepared for modeling. ArcGIS pro was used to calculate the slope at each hidden danger point, represented by a color gradient to highlight the varying steepness. Python's

edge detection algorithms identified terrain cracks from satellite images, providing detailed surface fracture data.

To enhance model training, the extracted slope and crack features are combined using layer superposition based on their spatial relevance. This integration resulted in a comprehensive training dataset that accurately captured these essential features, enabling the creation of fully recognizable training images for the model (Figure 5).

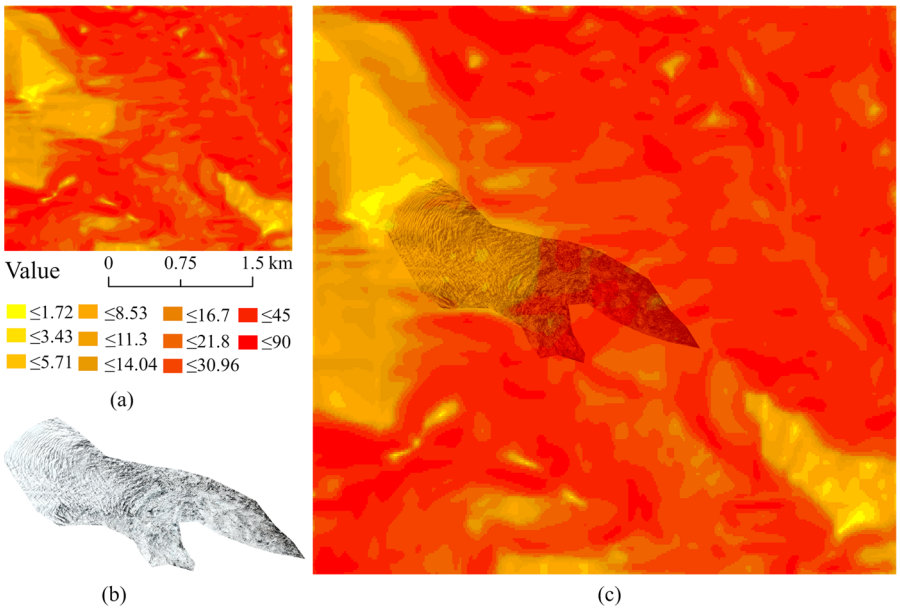

Figure 5. IA hidden danger feature fusion and training images. (**a**) The steepness of the slope increases as the color transitions from yellow to red, indicating a change from a gentle to a steep gradient; (**b**) The crack in the glacier IA area; (**c**) The training set image that integrates slope and cracks for comprehensive visualization.

3.2. Identification Index and Danger Levels Classification of IA

By integrating remote sensing data with geospatial techniques, and focusing on IA characteristics in typical case areas, key factors such as slope and crack distribution are examined to develop an index system for IA hidden danger identification, and several typical cases are used for comparative validation. Finally, IA hidden danger levels are classified based on slope and crack development.

3.2.1. Characteristics of Typical IA

Based on the remote sensing images from the Resource No.3 02 satellite on 22 December 2016, 28 December 2017, and 30 December 2018 (Figure 4), the Sedongpu Basin was divided into nine independent snow and ice accumulation zones (regions ①–⑨) during the pre-avalanche period. The classification was primarily derived from remote sensing imagery and topographic characteristics, including glacier recharge areas, deformation body distribution, movement directions, and terrain features (detailed in Table 2). The stability of each glacier and the hidden danger of an IA was assessed based on slope and crack distribution.

Since 2014, the Sedongpu Glacier has experienced continuous evolution. By December 2016, numerous cracks had developed within the glacier's deformation bodies. By December 2017, these cracks expanded further and penetrated the glacier surface. In 2018, the continued expansion of these cracks triggered an IA, resulting in significant debris flow, blocking the river and causing large-scale sliding. Figure 6 illustrates the critical role of cracks in inducing IAs.

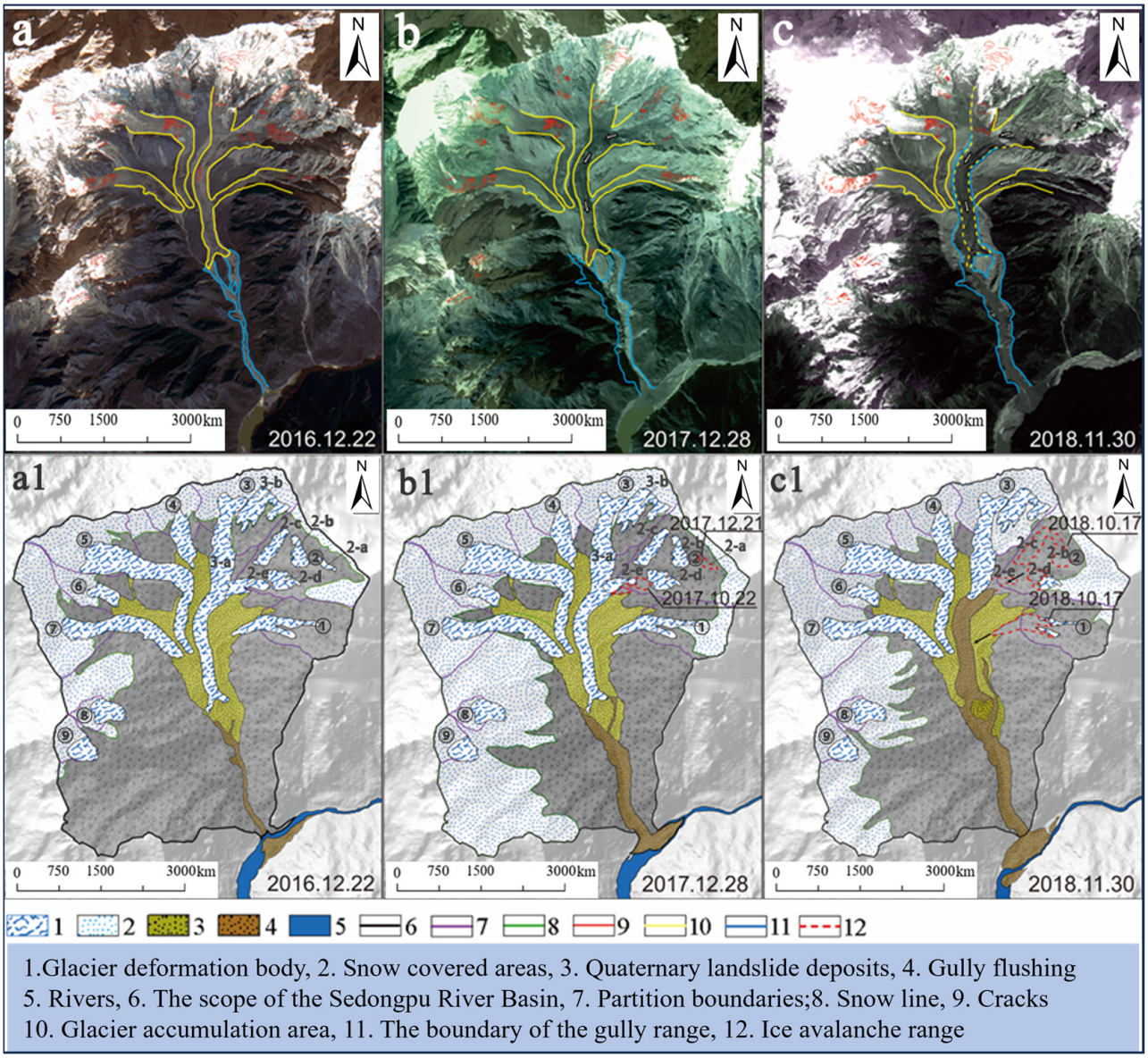

Figure 6. Development of IA in the Sedongpu Valley. (**a**–**c**) Shows satellite images of the Sedongpu Valley on different dates in 2016, 2017, and 2018, highlighting changes in glacier flow and landslide areas; (**a1**–**c1**) Corresponding schematic maps for the same dates, marking regions such as glacier flow, snow cover, river channels, and landslide debris.

In addition, by processing the digital elevation model (DEM) of the Sedongpu Glacier as of 22 December 2016, and performing slope calculations using ArcGIS, a direct correlation between slope and IA occurrence was identified. Figure 7 shows the proportion of glacial deformation in different slope intervals, with yellow to red areas representing slopes steeper than 30°. In regions ① and ②, the average slope of areas prone to frequent IAs ranged between 30° and 60°. A higher proportion of glacier deformation areas with slopes exceeding 30° is linked to an increased likelihood of IA events. In particular, the upstream residual glacier deformation area in region ③ shows a significant average slope and a notable proportion of areas with slopes over 30°.

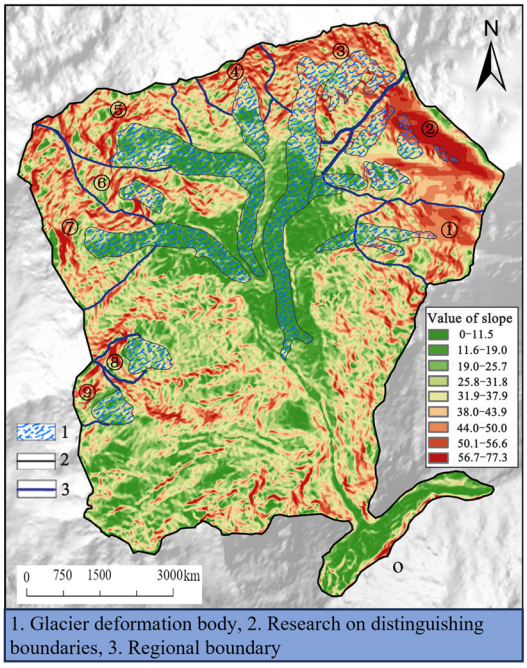

Figure 7. The slope zoning statistics of the Sedongpu Valley.

Table 2. Glacier slope information statistics in the Sedongpu Valley.

Glacier Zoning	Description and Division Basis	Average Slope	The Proportion of Area Exceeding 30°
①	Formed by two converging valleys, with tension cracks at the rear and middle. Division based on recharge and deformation features.	27.66°	26.05%
②	Contains five glacier deformation bodies, divided by crack distribution and movement direction, with fractures at the front in some areas.	20.27–57.66°	13.20–50%
③	Contains two glacier deformation bodies, gentle in front and steep at the rear. Slope and cracks are key monitoring factors, divided based on upstream residual glacier slope and deformation.	20.02–34.61°	19.67–45.7%
④	The single glacier deformation body follows the slope, with tension cracks at the rear and a steep front. Division based on slope and crack distribution	26.38°	27.14%
⑤	It has a curved shape with many cracks at the bend. Divided by terrain and crack distribution. The front is parallel to but not connected with the main channel.	18.52°	8.28%
⑥	The glacier is funnel-shaped with a gentle slope and minor cracks at the rear. Division based on distinct terrain features.	29.08°	30.91%
⑦	An independent glacier with significant rear deformation and concentrated cracks. Division based on crack and deformation characteristics.	16.15°	3.64%
⑧	Far from the main channel with significant elevation difference. Division based on terrain variation from the main channel.	27.16°	24.95%
⑨	Minor tension cracks at the rear and clear runoff traces at the front. Division based on slope and crack features.	25.41°	17.90%

3.2.2. Identification Index

The Sedongpu No. 6 Glacier in China serves as the primary focus, from which remote sensing images are used to examine glacial IA events. To further validate the

universality of the findings, data from the Chamoli region in India (7 February 2021) [32] and the Monte Maldarà region in Italy (3 July 2022) [33] are also compared. The Sedongpu Glacier's satellite images from 4 December 2017 revealed significant slope angles and tensile cracks (Figure 8a). Similarly, images from the Chamoli glacier (5 February 2021) and the Marmolada glacier (3 July 2022) (Figure 8b,c) show comparable patterns of steep slopes and crack development. These comparisons are made to reinforce that slope steepness and crack formation are universal precursors to glacial disintegration and IA events, observed across different regions.

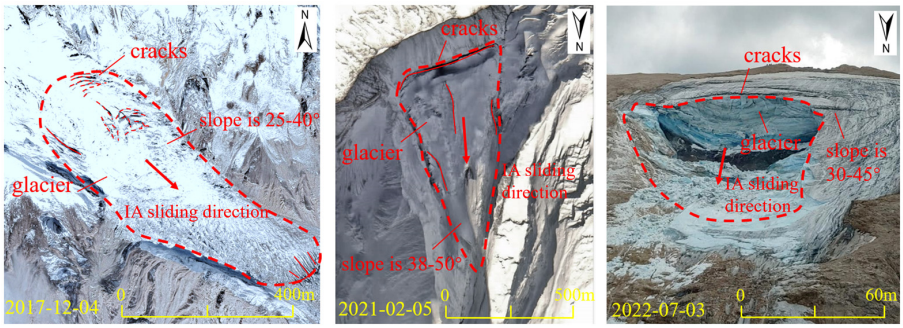

Figure 8. Slope and crack evolution processes in different glacier source areas. (**a**) Slope and cracks in the Sedongpu glacier source area (4 December 2017); (**b**) Slope and cracks in the Chamoli glacier source area (5 February 2021); (**c**) Slope and cracks in the Marmolada glacier source area (Photo provided by Italy's Alpine Rescue on 3 July 2022) (Google earth pro. Map. Retrieved from: https://www.google.com/earth/, accessed on 8 July 2024).

Figure 6 illustrates the slope and crack distribution across these glaciers. IA hidden danger areas are highlighted with red ellipses, derived from remote sensing interpretation and slope calculations using DEM data. Cracks are emphasized with red lines to indicate areas most vulnerable to disintegration. For the Sedongpu glacier (Figure 8a) and Chamoli glacier (Figure 8b), prominent cracks are observed in steep sections, indicating high-hidden danger IA zones. Similarly, the Marmolada glacier (Figure 8c) shows crack expansion in steep regions, indicating potential future disintegration.

These comparisons confirm that despite geographical differences, steep slopes and crack propagation are consistent indicators of IA hidden danger. These findings, observed through the remote sensing of the Sedongpu Glacier, are reinforced by the results from Chamoli and Marmolada, demonstrating that slope steepness and crack expansion are reliable precursors to IA events.

In summary, identifying IA hidden danger areas relies on evaluating three key indicators: source glacier, steep slope, and cracks (Figure 9).

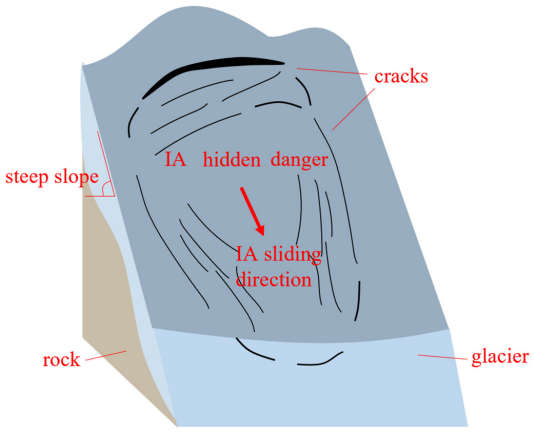

Figure 9. Schematic conceptual diagram of IA hidden danger.

3.2.3. Danger Levels Classification

Based on statistical data on 40,269 glaciers on the TP, IA development follows a normal distribution relative to slope [34]. The sensitive slope range for IA development is between 35° and 55°, accounting for 95% of the total number of IA hidden danger. When the slope is less than 25° or greater than 55°, the number of IA hidden danger decreases significantly [2]. At lower slopes, insufficient potential energy prevents sliding, while steeper slopes increase stability, reducing the chance of collapse. Herein, slope is divided into three IA danger levels, low (<25°), medium (25–55°), and high (>55°) [2,18].

Crack development is classified by factors such as the number of crack groups, density, width, and extension length [35]. Weakly developed cracks have fewer than five groups with sparse distribution and small openings, indicating low danger. Moderately developed cracks (5–10 groups) show moderate density and extension, signaling increased instability. Strongly developed cracks (over 10 groups) have dense distribution, large openings, and long extensions, indicating high collapse danger [36].

IA danger levels are determined by both slope and crack development. Low danger occurs when both are low, medium danger when both are moderate, and high danger when both are high. A moderate slope with strong crack development can also elevate the danger level (Table 3).

Table 3. Classification criteria for IA hidden danger Levels.

Danger Level / Slope Angle / Crack	Low Slope (<25°)	Medium Slope (25–55°)	High Slope (>55°)
Weak development	Low	Low	Medium
Medium development	Low	Medium	High
Strong development	Medium	High	High

3.3. Model Construction for Artificial Intelligent Identification

3.3.1. Construction Principle

ResNet50, developed by Kaiming He and colleagues at Microsoft Research in 2015, addresses degradation in deep neural network training [37]. As network depth increases, performance typically improves, then saturates, and may decline. ResNet50 introduces a residual learning structure, where each block has a shortcut connection that bypasses one or more layers. Through this, the network learns residual mappings instead of direct mappings, mitigating vanishing and exploding gradients, and enhancing training efficiency and model accuracy [38].

The architecture begins with a 7 × 7 convolutional layer (stride of 2), followed by batch normalization, a ReLU activation layer, and max pooling. Subsequent layers include four groups of residual blocks, each containing multiple blocks with three convolutional layers (1 × 1, 3 × 3, 1 × 1) to reduce complexity [39]. Each block includes batch normalization and ReLU activation, with jump connections linking the blocks. The design concludes with a global average pooling layer to reduce parameters and minimize overfitting risk, followed by a fully connected layer and a Softmax layer for output (Figure 10a). The skip connections significantly enhance training stability and model accuracy.

VGG, an advanced CNN model based on TensorFlow, was first proposed by Simonyan and Zisserman in 2014 [40]. It plays a crucial role in deep learning and data mining, particularly in high-precision classification and prediction [41]. The model features 3 × 3 convolutional kernels and a streamlined architecture. It includes multi-layer nonlinear processing layers to enhance the learning of complex patterns, making it ideal for image recognition and classification. VGG16, a variant of the VGG series, illustrated in Figure 10b, consists of thirteen convolutional layers and three fully connected layers. It accepts a 224 × 224 pixel RGB image, starting with two convolutional layers of 64 kernels each, followed by ReLU activation to maintain spatial resolution [42]. The subsequent

2 × 2 max pooling layer reduces the feature map size progressively. As the network deepens, the number of convolution kernels increases to 128, 256, and 512, allowing in-depth feature extraction. The model culminates in a 7 × 7 × 512 feature map passing through three fully connected layers, and a 1000-unit output layer employing the Softmax function for final classification [43,44].

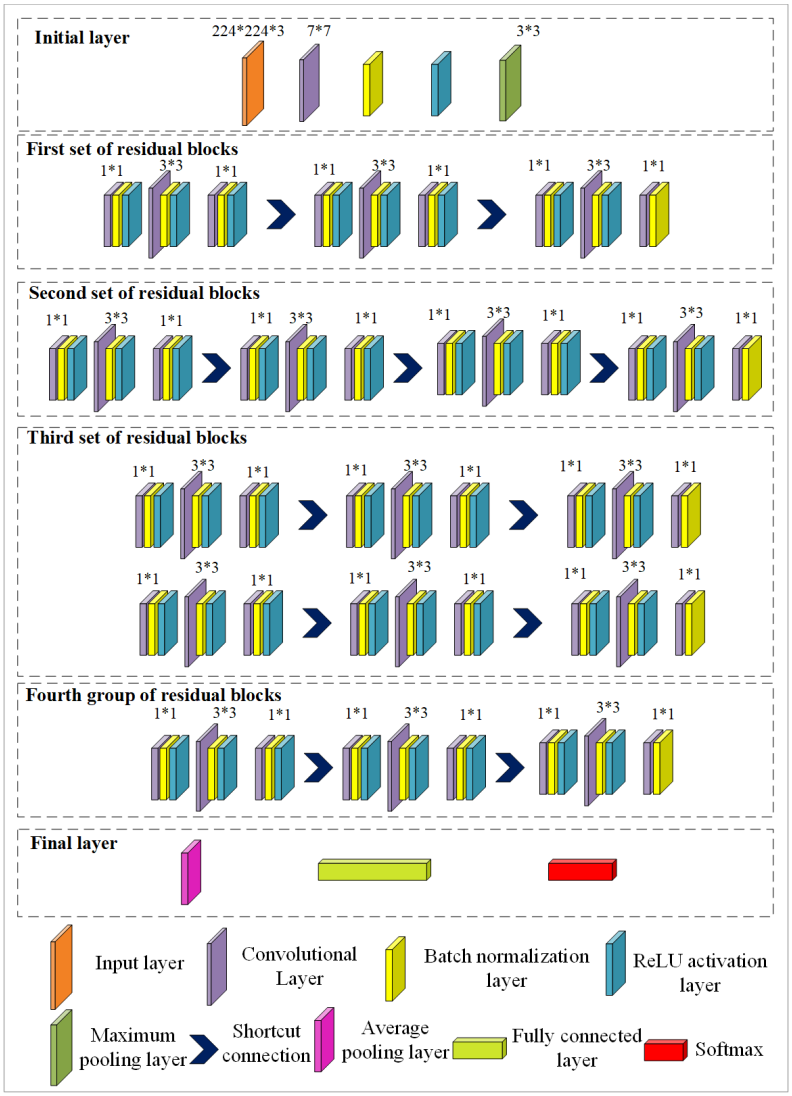

(**a**)

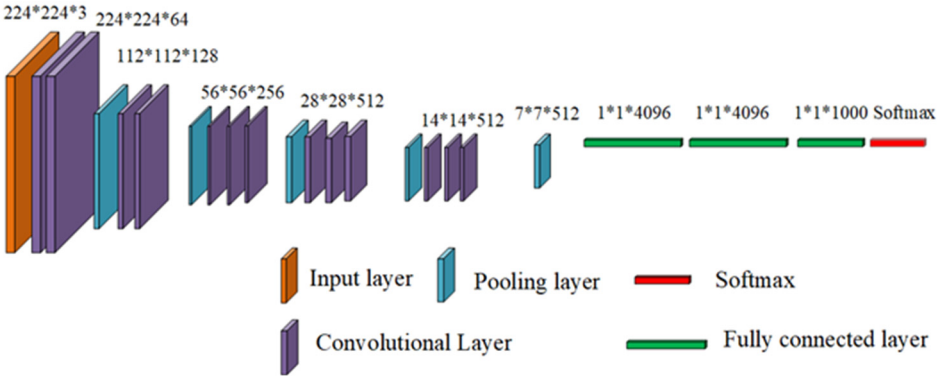

(**b**)

Figure 10. Model construction principal processes: (**a**) ResNet50 model network architecture; (**b**) VGG16 model network structure.

3.3.2. Parameter Setting and Model Training

This study employed detailed data preprocessing techniques to ensure the quality and reliability of the 1081 samples, consisting of 581 identified IA hidden danger point samples and 500 UA samples. These samples are divided into training and test sets in an 8/2 ratio, with 20% of the training set reserved for validation (Table 4). The image preprocessing steps included resizing the images to 224 × 224 pixels, random shuffling, and normalizing pixel values between 0 and 1, thereby improving model convergence and stability.

Table 4. IA hidden danger model training sample division.

Sample Name	Total Quantity	Training Set Quantity (Proportion)	Validation Set Quantity (Proportion)	Test Set Quantity (Proportion)
IAs UAs	581 500	692 (64%)	173 (16%)	217 (20%)

To prevent overfitting and optimize the training process, careful settings were chosen for learning rates, epochs, and batch sizes. The ResNet50 model used the Adam optimizer, which adaptively adjusts the learning rate based on the training progress, with no fixed settings for epochs or batch size, allowing for greater flexibility during training. In contrast, the VGG16 model used the SGD optimizer, requiring precise settings for the learning rate, epochs, and batch size to achieve optimal training performance.

3.3.3. Performance Evaluation

Six key indicators are selected to ensure the comprehensive and accurate assessment of the performance of two models, Accuracy (Acc), Loss rate (Loss), Precision (Pre), Recall rate (Rec), F1 score ($F1_{score}$), and Model Run Time (Time). These metrics measure the performance of the model on the training, validation, and test sets, and reflect its performance in dealing with different categories in the dataset.

Specifically, Acc is the proportion of instances correctly predicted by the model, which reflects the predictive ability of the model. Loss quantifies the deviation between the model prediction and the actual label, a statistical measure of the error. The Pre, Rec, and F1 $_{score}$ are calculated based on the Confusion Matrix (CM) and return the recognition accuracy, recall rate, and F1 $_{score}$ for each type of data sample. The correlation expression is presented below. All evaluation metrics are derived from the confusion matrix (CM), which categorizes prediction results into True Positives (*TP*), True Negatives (*TN*), False Positives (*FP*), and False Negatives (*FN*). A detailed description is provided in Table 5.

$$\text{Acc} = \frac{NP}{OS} \tag{1}$$

$$\text{Loss} = -\frac{1}{N}\sum_{i=1}^{N}[y_i \cdot \log(\hat{y}_i) + (1 - y_i) \cdot \log(1 - \hat{y}_i)] \tag{2}$$

$$\text{Pre} = \frac{TP}{TP + FP} \tag{3}$$

$$\text{Rec} = \frac{TP}{TP + FN} \tag{4}$$

$$F1_{score} = 2 \cdot \frac{\text{Pre} \cdot \text{Rec}}{\text{Pre} + \text{Rec}} \tag{5}$$

For the loss function, Loss utilizes Binary Cross-Entropy for computation; *NP* is the number of correctly identified samples; *OS* is the total number of samples; and *N* represents the number of samples. Moreover, y_i is the actual label of the sample and $\hat{y}_i$ is the predicted probability of the model.

Table 5. Description of model performance indicators.

Name	Symbol	Description
Accuracy	Acc	The number of correctly classified samples divided by the total number of samples.
Loss rate	Loss	The loss rate measures the inconsistency between model predictions and actual values.
Precision	Pre	Precision is the ratio of true positives to all predicted positives.
Recall	Rec	Recall is the ratio of true positives to all samples that should be identified as positive.
F1 *score*	$F1_{score}$	The harmonic mean of precision and recall evaluates their balance in a model.
True positive	*TP*	The model correctly identifies positive samples.
True negative	*TN*	The model correctly identifies negative samples.
False positive	*FP*	The model incorrectly identifies negative samples as positive.
False negative	*FN*	The model incorrectly identifies positive samples as negative.
Macro average	MA	Average values of Pre, Rec, and F1 *scores* are calculated.
Weighted average	WA	Pre, Rec, and F1 *scores* are calculated by weighting the proportion of each sample.
Runtime	Time	Total runtime from model start to training completion.

To carefully evaluate the performance of the model in each category, training set accuracy rate (train_acc), training set loss rate (train_loss), validation set accuracy rate (valid_acc), validation set loss rate (valid_loss), test set accuracy rate (test_acc), and test set loss rate (test_loss) are used to evaluate the model. At the same time, the Macro Average (MA) and Weighted Average (WA) methods are used to calculate the macro average (MAA) and weighted average (WAA) of precision, the macro average (MAR) and weighted average (WAR) of recall, and the macro average (MAF) and weighted average (WAF) of F1 *score*. Table 6 shows the model's overall performance evaluation indicators. It reveals the adaptability and precision of the model when facing datasets with unevenly distributed categories.

$$\mathrm{MAA} = \frac{1}{n}\sum_{i=1}^{n}\mathrm{Acc}(C_i) \tag{6}$$

$$\mathrm{MAR} = \frac{1}{n}\sum_{i=1}^{n}\mathrm{Rec}(C_i) \tag{7}$$

$$\mathrm{MAF} = \frac{1}{N}\sum_{i=1}^{n}\mathrm{F1_{score}}(C_i) \tag{8}$$

$$\mathrm{WAA} = \sum_{i=1}^{n}\left(\frac{N_i}{\sum_{j=1}^{n} N_j}\right)\cdot\mathrm{Acc}(C_i) \tag{9}$$

$$\mathrm{WAR} = \sum_{i=1}^{n}\left(\frac{N_i}{\sum_{j=1}^{n} N_j}\right)\cdot\mathrm{Rec}(C_i) \tag{10}$$

$$\mathrm{WAF} = \sum_{i=1}^{n}\left(\frac{N_i}{\sum_{j=1}^{n} N_j}\right)\cdot\mathrm{F1_{score}}(C_i) \tag{11}$$

In this context, n represents the number of categories, C_i denotes the i-th category, and N_i represents the number of samples in the i-th category.

Table 6. Model performance evaluation indicators.

Key Indicators	Evaluation Indicators	Symbol
Acc	Training set accuracy rate	train_acc
	Validation set accuracy rate	valid_acc
	Test set accuracy rate	test_acc
Loss	Training set loss rate	train_loss
	Validation set loss rate	valid_acc
	Test set loss rate	test_loss
Pre	Accuracy per class	IAS
	Macro average accuracy	MAA
	Weighted average accuracy	WAA
Rec	Recall per class rate	RES
	Macro average recall rate	MAR
	Weighted average recall rate	WAR
$F1_{score}$	F1 $_{score}$ per class	FES
	Macro average F1 $_{score}$	MAF
	Weighted average F1 $_{score}$	WAF
Time	Model runtime	Time

3.3.4. Model Training Results

The diagnostic performance of the models was evaluated using the Acc curve, with identification accuracy and loss rates for different epochs shown in Figures 11 and 12. The ResNet50 model achieved optimal performance after 10 epochs, with a batch size of 128. On the other hand, the VGG16 model reached its peak performance at 18 epochs, with a learning rate of 0.001 and a batch size of 128.

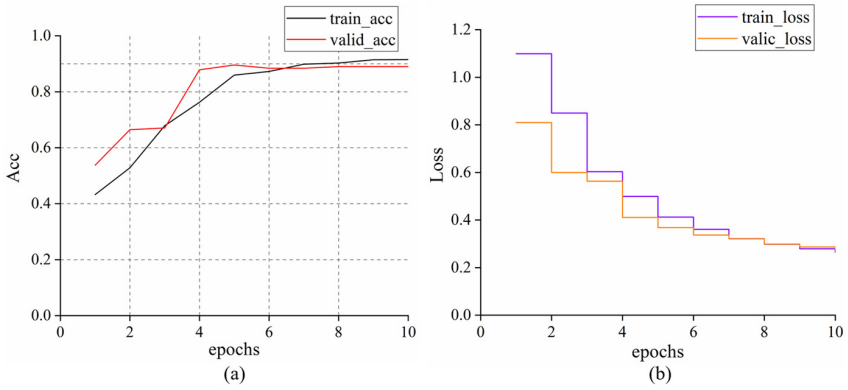

Figure 11. ResNet50 model training results: (**a**) Model accuracy; (**b**) Model loss rate.

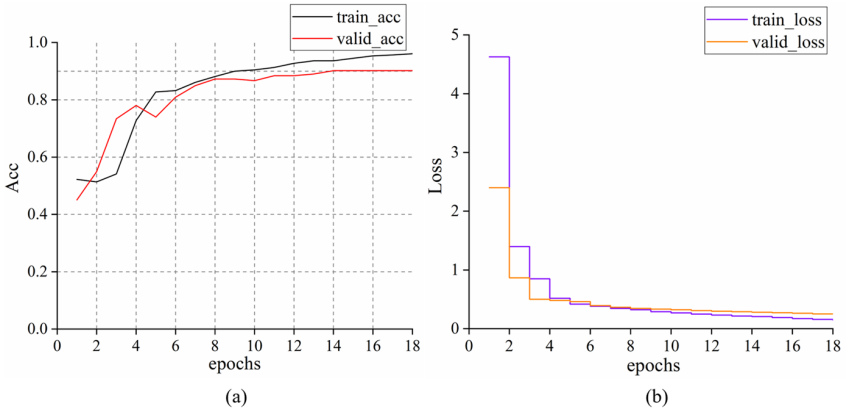

Figure 12. VGG16 model training results: (**a**) Model accuracy; (**b**) Model loss rate.

The confusion matrix in Figure 13 and the performance metrics in Table 7 further illustrate the comparison between the ResNet50 and VGG16 models in terms of training and validation accuracy. While VGG16 outperformed ResNet50 in the training and validation phases, it lagged slightly behind in the test set performance. This suggests that, although VGG16 demonstrated strong capabilities in identifying IA hidden danger, further optimization is required to enhance its accuracy and efficiency on unseen data.

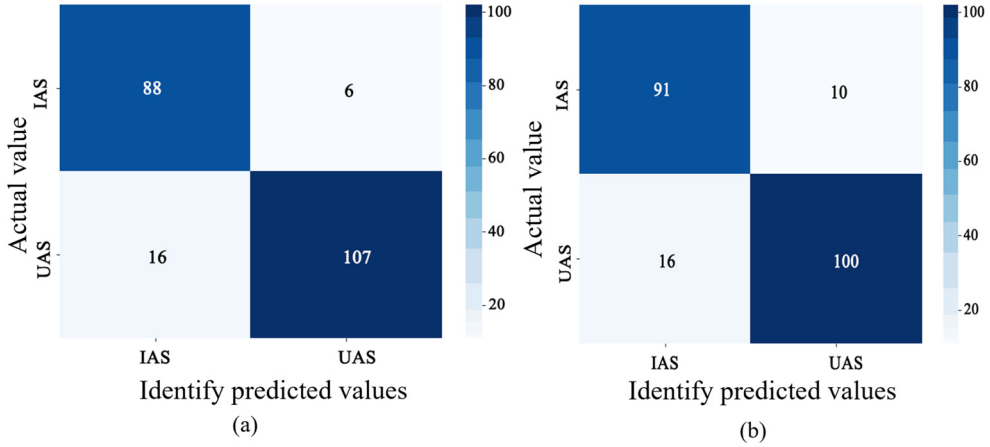

Figure 13. CM for model test set recognition results: (**a**) ResNet50; (**b**) VGG16.

Table 7. Model specific training results.

Indicators \ Models	ResNet50	VGG16
train_acc	0.9132	0.9609
valid_acc	0.8902	0.9017
test_acc	0.8986	0.8802
train_loss	0.2644	0.1479
valid_loss	0.2788	0.2532
test_loss	0.2589	0.2801
IAS	0.85/0.95	0.85/0.91
MAA	0.9	0.88
WAA	0.9	0.89
RES	0.94/0.87	0.90/0.86
MAR	0.9	0.89
WAR	0.9	0.88
FES	0.89/0.91	0.88/0.88
MAF	0.9	0.88
WAF	0.9	0.88
Time (min)	4	15

3.3.5. Model Optimization

The VGG16 model was optimized for identifying IA hidden danger using pre-optimization measures such as data enhancement, Early Stopping (ES), and L2 Regularization. While data enhancement typically boosts generalization, it was found that in this specific task, the data-enhanced model (D-VGG16) absorbed excessive noise from over-processed training samples, reducing accuracy (Figure 14). Conversely, the ES-VGG16 model effectively prevented overfitting and shortened the training cycle by terminating when validation set loss ceased to decrease, as illustrated in Figure 15. Additionally, the introduction of L2 Norm Regularization (L2-VGG16) significantly enhanced performance on both training and test sets and reduced overfitting risks (Figure 16), with related indicators such as Precision and Recall detailed in Table 8.

By integrating Early Stopping and regularization, the optimized ES-L2-VGG16 model demonstrated improved accuracy, operational efficiency, and faster convergence in identifying IA hidden danger, as shown in Figure 17. The experience with VGG16 underscores

the importance of selecting appropriate optimization strategies, tailored to the model's structure and task requirements. Understanding the adaptability of different technologies across various model architectures is crucial for effective optimization.

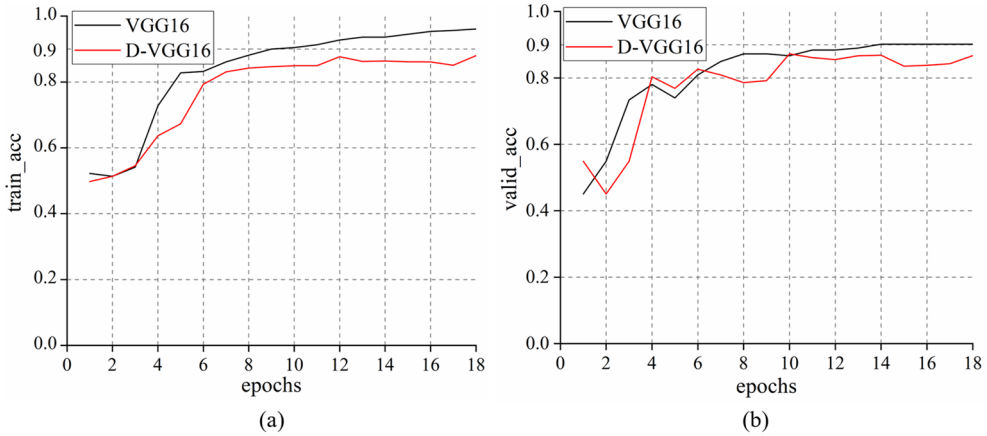

Figure 14. Comparison of accuracy between VGG16 and D-VGG16 models: (**a**) Training set accuracy; (**b**) Validation set accuracy.

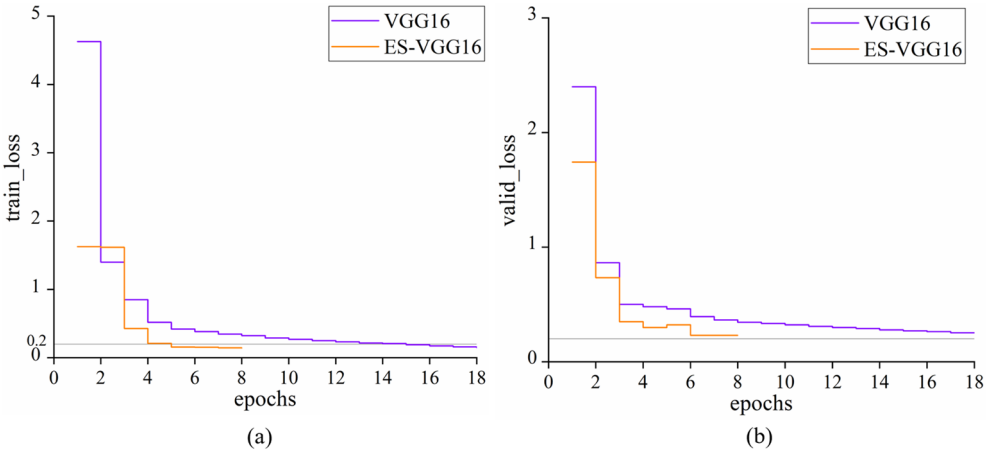

Figure 15. Comparison of loss rate between VGG16 and ES-VGG16 models: (**a**) Training set loss; (**b**) Validation set loss.

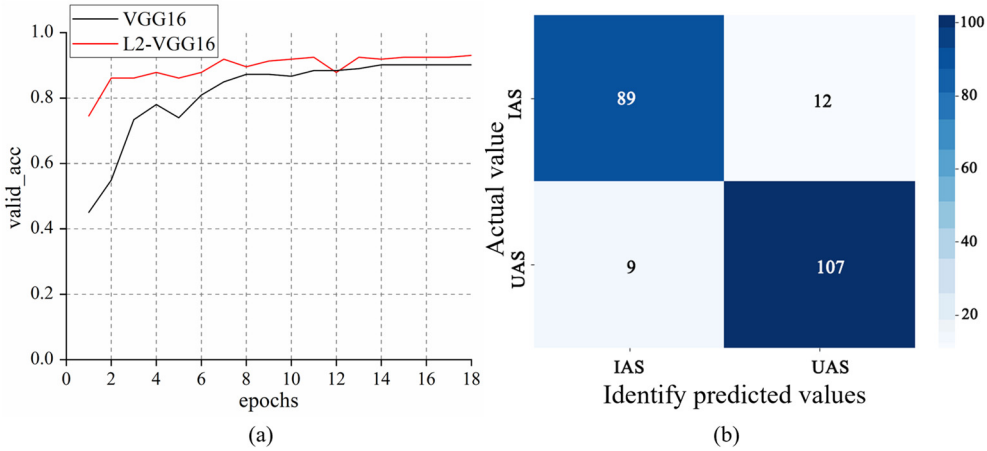

Figure 16. Training performance of the L2-VGG16 model on validation and test sets: (**a**) Validation set accuracy of VGG16 and L2-VGG16 models; (**b**) L2-VGG16 model test set training results.

Table 8. Specific metrics of models with different optimization strategies.

Metrics \ Models	D-VGG16	ES-VGG16	L2-VGG16	ES-L2-VGG16
train_acc	0.8799	0.9687	0.9776	0.9861
valid_acc	0.8674	0.9075	0.9306	0.9306
test_acc	0.8731	0.8756	0.8940	0.8940
train_loss	0.2741	0.1425	0.0504	0.0338
valid_loss	0.2518	0.231	0.2178	0.2097
test_loss	0.2825	0.2721	0.2747	0.2611
IAS	0.88/0.89	0.86/0.90	0.91/0.88	0.88/0.91
MAA	0.8	0.87	0.90	0.90
WAA	0.8	0.89	0.89	0.89
RES	0.87/0.89	0.90/0.86	0.90/0.92	0.90/0.92
MAR	0.8	0.88	0.89	0.89
WAR	0.8	0.88	0.89	0.89
FES	0.87/0.88	0.87/0.88	0.88/0.90	0.89/0.90
MAF	0.88	0.88	0.89	0.89
WAF	0.88	0.88	0.89	0.89
Time(min)	15	7	13	10

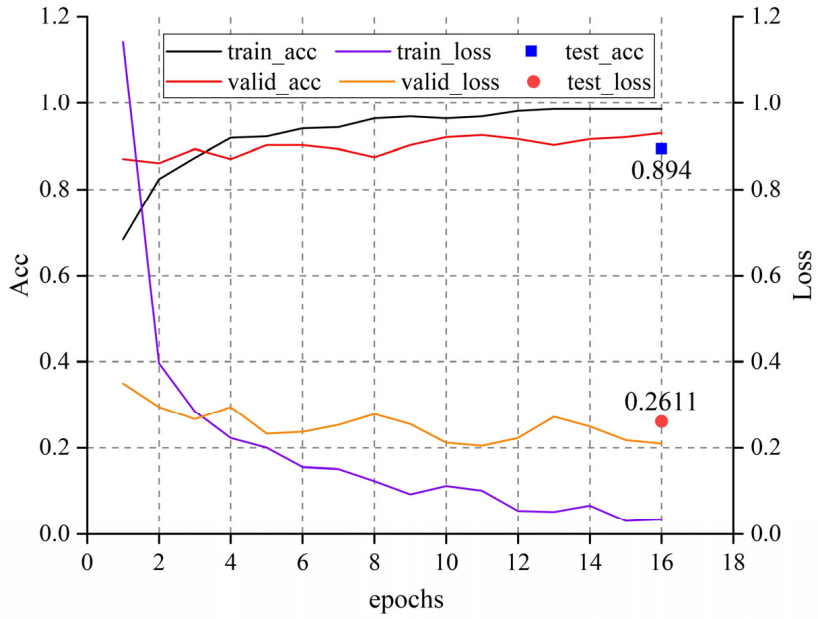

Figure 17. Training results of the ES-L2-VGG16 model.

3.4. Identification Procedure of IA Hidden Danger

In identifying IA hidden danger, the process starts with the efficient detection of source glaciers in the target region using advanced machine vision technology, where the boundaries are clearly marked with green contour lines.

Subsequently, the optimized ES-L2-VGG16 deep neural network model accurately identifies cracks in the glacier source area, marking these with red ellipses based on the model's learned characteristics of glacier cracks and slopes.

Meanwhile, slopes within the glacier area are meticulously measured and translated into pixel values using GIS technology, with the data derived from Sentinel-2A satellite images and analyzed using ArcGIS and Google Earth pro 7.3.6 software. Pretrained by the model, slope features are automatically recognized and highlighted with blue rectangles to assess the area's slope status, as detailed in Figure 18.

In Figure 18c, the intersection of glacier boundaries (marked in green), cracks (marked with red ellipses), and slope markings (highlighted with blue rectangles) ultimately represents the identified IA hidden danger areas. The regions labeled "p1–p8" correspond to specific locations within the glacier, where the model identified critical combinations of these indicators, marking them as areas with hidden danger of IA.

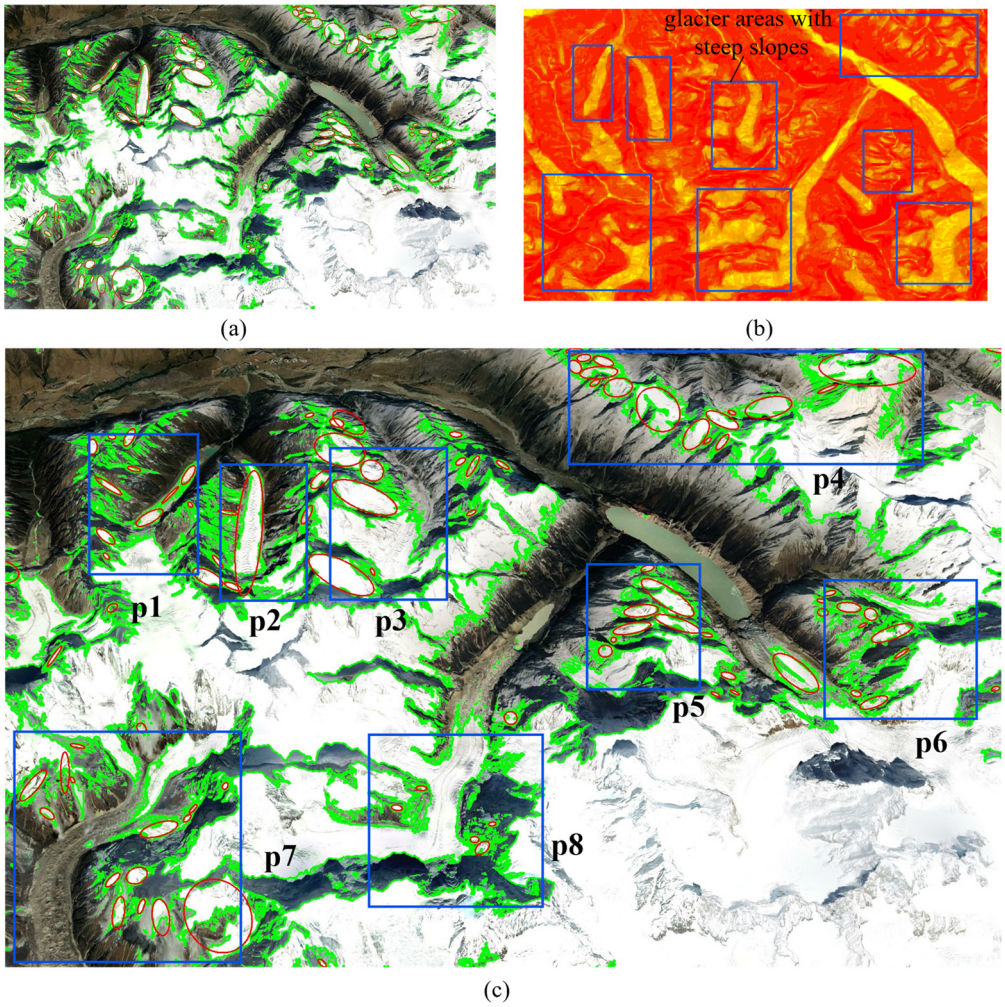

Figure 18. IA hidden danger identification process overview: (**a**) A satellite image of a glacier, with glacier boundaries marked in green and identified cracks is highlighted by red ellipses; (**b**) Gradient changes in the glacier area are marked by blue rectangles indicating slopes; (**c**) The area where the green boundary, red ellipse, and blue rectangle intersect is an IA hidden danger area. (Google earth pro. Map. Retrieved from: https://www.google.com/earth/, accessed on 15 July 2024).

In addition, the slope features are extracted at the pixel level, which allows for the precise measurement of slope variations across the glacier surface. For crack detection, an edge detection algorithm is employed to accurately identify and extract cracks. The process of extracting and analyzing slope and crack features is shown in Figure 19.

Ultimately, this comprehensive integration of glacier boundaries, cracks, and slope data enables the precise identification of hidden danger, allowing IA hidden danger areas to be located more efficiently and accurately during the glacier identification and validation process.

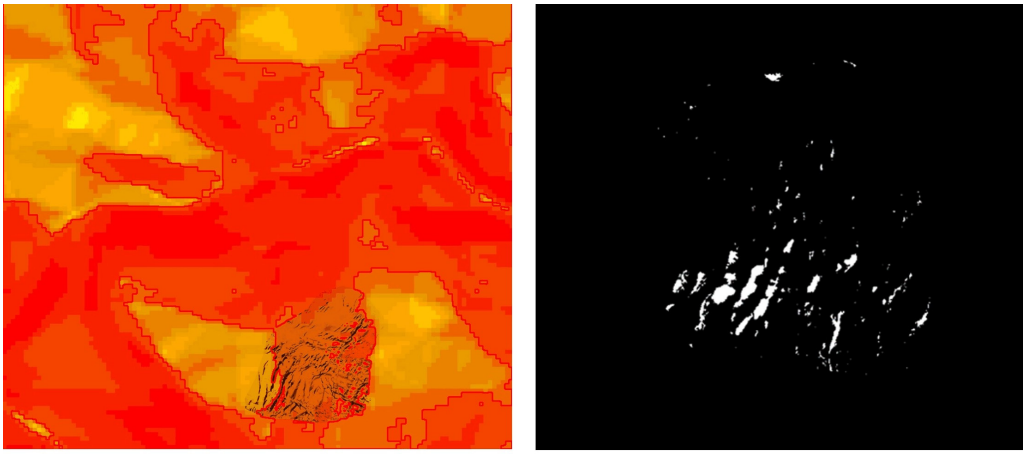

(a) (b)

Figure 19. Extraction process: (**a**) Slope recognition process; (**b**) Crack extraction process.

4. Results

4.1. Identification Results

Based on the identification methods applied in this research, a systematic evaluation of IA hidden danger in the glacier-dense region of the Yarlung Tsangpo River Gorge was conducted. A total of 100 IA hidden danger areas were identified, with 48% classified as high danger areas, 36% as medium danger areas, and 16% as low danger areas, as illustrated in Figure 20. The average slope of medium- and high-danger areas ranges from 34° to 48°, with crack development predominantly found in the steep terrains of the Yarlung Tsangpo River Gorge. Further detailed information is provided in Supplementary Table S1.

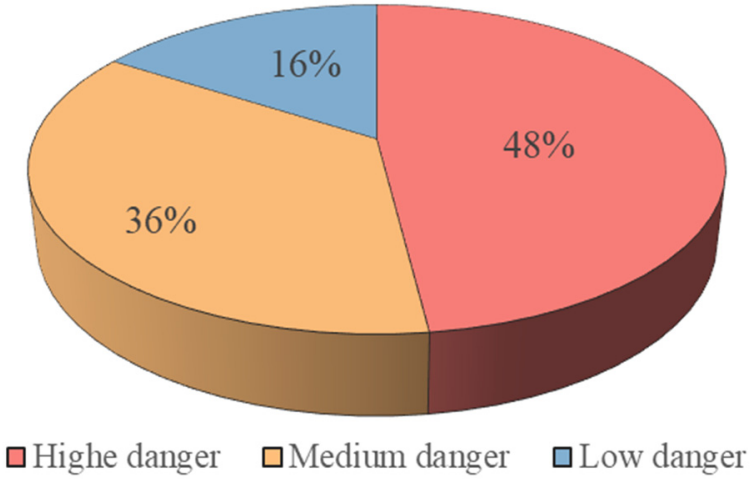

Figure 20. Distribution of IA danger levels in the Yarlung Tsangpo River Gorge.

Based on a comprehensive assessment of glacier boundaries, slopes, and crack distribution, the spatial distribution and danger levels of IA hidden danger areas in the Yarlung Tsangpo River Gorge were precisely identified. The locations of these hidden danger areas were clearly determined, and each area's hidden danger level was systematically classified. The relevant results are presented in Figure 21, where the yellow, purple, and red circles indicate the preliminary identified danger levels of hidden IAs, clearly illustrating the danger distribution across the different areas.

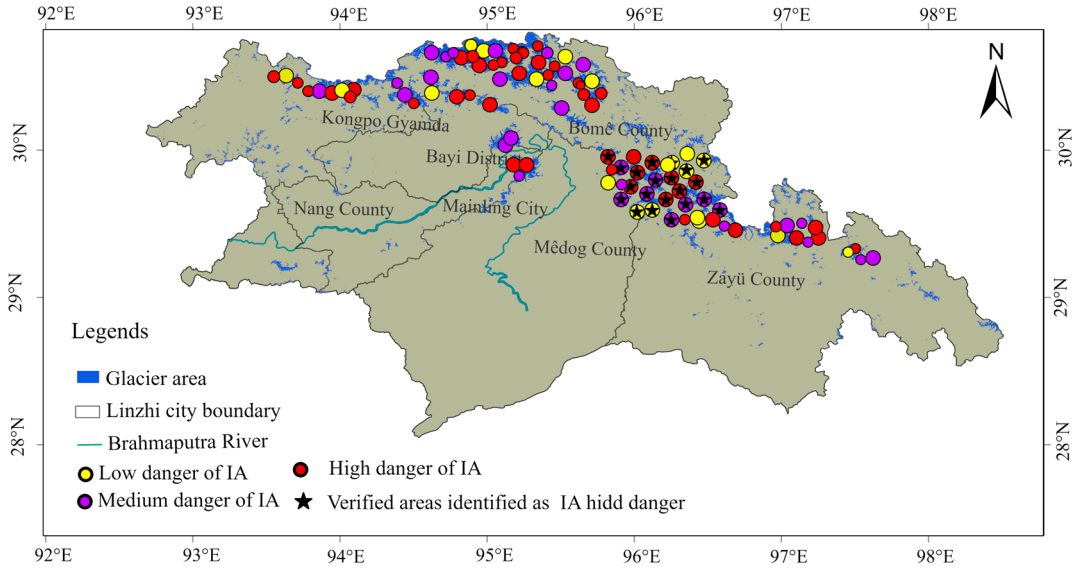

Figure 21. IA hidden dangers identification and verification results.

4.2. Validation and Verification

To verify the accuracy of the identification of the IA hidden danger areas, the 25 regions identified earlier are selected for verification. A 12.5 m resolution DEM, covering a 5 km radius around each glacier area, is used to extract key terrain parameters such as slope. An edge detection algorithm then identifies crack information for constructing a verification sample set of IA hidden dangers. Using these data, the ES-L2-VGG16 model is trained to discern and verify whether glacier areas pose IA hidden dangers. The verification results are displayed in Figure 21, where the black star indicates the area confirmed as an IA hidden danger through the verification process.

The discrimination process relies on glacier characteristics such as slopes and cracks, with a threshold set at 0.5. Areas exceeding this threshold are classified as IA hidden danger areas, while others are considered safer. Table 9 presents the verification results for the 25 glacier areas.

To further verify the accuracy of the identification, the model's verification results are compared with the detailed remote sensing interpretations of the same glacier regions. For example, Figure 22 shows the identification results and satellite interpretations for two areas, (1) and (2). Comparative results revealed that the IA hidden danger identified by the model are consistent with satellite interpretations.

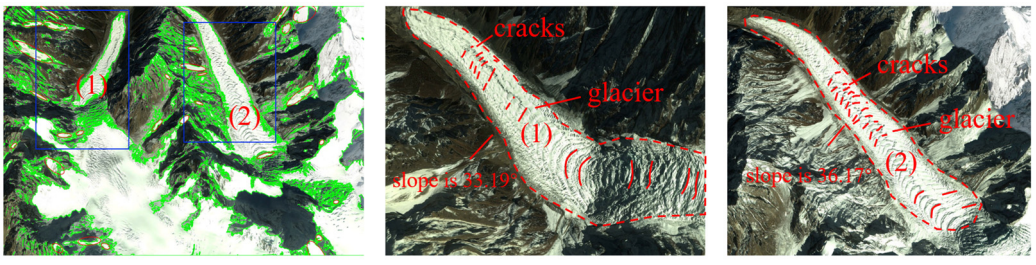

Figure 22. Remote sensing interpretation of glacier areas: (**a**) Automatic identification results for regions (1) and (2); (**b**) Remote sensing satellite image of area (1); (**c**) Remote sensing satellite image of area (2) (Google earth pro. Map. Retrieved from: https://www.google.com/earth/, accessed on 12 July 2024).

Table 9. Discrimination results for glacier areas.

No.	Glacier Area	Identified as Hidden Danger Areas	Standard Threshold	Verify Recognition Threshold	Verify Consistency of Identification with Remote Sensing Images	Verify Identification Accuracy
1	p1	Yes		0.53	Yes	
2	p2	Yes		0.52	Yes	
3	p3	Yes		0.55	Yes	
4	p4	Yes		0.58	Yes	
5	p5	Yes		0.59	Yes	
6	p6	Yes		0.53	Yes	
7	p7	Yes		0.56	Yes	
8	p8	Yes		0.53	Yes	
9	p9	No		0.43	Yes	
10	p10	Yes		0.52	Yes	
11	p11	Yes		0.55	Yes	
12	p12	Yes		0.56	Yes	
13	p13	Yes	0.5	0.53	Yes	96%
14	p14	Yes		0.52	Yes	
18	p15	No		0.45	Yes	
16	p16	Yes		0.53	Yes	
17	p17	Yes		0.52	Yes	
18	p18	No		0.46	Yes	
19	p19	Yes		0.55	Yes	
20	p20	Yes		0.48	No	
21	p21	Yes		0.52	Yes	
22	p22	No		0.44	Yes	
23	p23	Yes		0.56	Yes	
24	p24	Yes		0.56	Yes	
25	p25	Yes		0.54	Yes	

5. Discussion

Recent research shows that deep learning algorithms have been widely used in predicting natural disasters, particularly landslides and IA hidden dangers. Liu et al. [45] and Li et al. [46] demonstrated that deep learning models outperform traditional methods. Deep learning models like CNN and VGG have been successfully applied to predicting geohazards such as landslides, IAs, and debris flows [47]. These models achieved assessment accuracies of 90% and 91.89% in identifying landslides and glaciers, respectively [48,49]. This verifies their feasibility and accuracy in natural disaster identification. However, traditional algorithms like logistic regression, SVM, MDA, BPNN, and RF, remain effective in specific scenarios [50–52]. Yet, in the complex terrain of the TP, these methods struggle to extract sufficiently accurate information.

In this paper, the ES-L2-VGG16 model was constructed by further improving the deep learning model with ES and L2. The data fusion method integrates multivariate data, such as slope and crack, achieving a training accuracy of 98.61%, which is significantly better than that of existing models. This highlights the importance of advanced deep learning strategies in improving model generalization and optimization. Consequently, the ES-L2-VGG16 model has become a powerful tool in natural disaster prediction.

Future research suggests focusing on optimizing the model to better recognize increasingly complex geological features and to expand the range of IA identification indicators to improve learning effectiveness. The model will integrate advanced algorithms such as DenseNet, Particle Swarm Optimization, and Long Short-Term Memory networks to enhance training accuracy and precision. The ultimate goal is to identify IA hidden danger in glacier regions worldwide, establish a comprehensive global IA hidden danger database, and provide support for identifying geological disasters.

6. Conclusions

(1) The key indicators for identifying IA hidden dangers were established, including glacier sources, steep slopes, and cracks, along with a danger level classification standard. The VGG16 identification model is selected and optimized, using Early Stopping (ES) to prevent overfitting and L2 regularization techniques (L2). An intelligent identification method for IA hidden danger based on deep learning is proposed.

(2) The research assessed the performance of VGG16 and ResNet50 models in identifying IA hidden danger. The superior VGG16 model was optimized to create the ES-L2-VGG16 model, tailored for the complex terrain and varying IA characteristics on the TP. Unlike traditional methods based on single images or color differences, this research employs GIS and deep learning technologies to analyze geological features such as slope and cracks. The identification process integrates multivariate data, enhancing the model's accuracy and reliability. The model achieved training, validation, and test accuracies of 98.61%, 93.06%, and 89.4%, respectively.

(3) In the application verification process in the Yarlung Tsangpo River Gorge in Nyingchi, the ES-L2-VGG16 model achieved a training accuracy of 98.61%. During the verification and identification of 25 IA hidden danger, the verification and identification accuracy was as high as 96%, accurately identifying hidden danger in glacier areas.

In summary, this research improves IA hidden danger identification accuracy and efficiency, establishing a foundation for deep learning in the early identification of natural disasters. Future work should enhance scalability and adaptability in complex environments.

Supplementary Materials: The following supporting information can be downloaded at: https://www.mdpi.com/article/10.3390/rs16214041/s1.

Author Contributions: Investigation, Methodology, Data curation, Software, Formal Analysis, Writing—original draft, and Validation, D.G.; Conceptualization, Methodology, Data curation, Resources, Supervision, Funding acquisition, Writing—review and editing, and Project administration, M.T.; Resources, Funding acquisition, and Project administration, Q.X. and G.W.; Formal Analysis, Writing—review and editing, G.L. and W.Y.; Data curation and Software, Z.L.; Investigation and Formal Analysis, H.Z.; Investigation and Visualization, Y.R. All authors have read and agreed to the published version of the manuscript.

Funding: This research was supported by the Second Tibetan Plateau Scientific Expedition and Research Program (STEP) under grant 2019QZKK0201, the National Natural Science Foundation of China under grant 42377199, Chengdu University of Technology Postgraduate Innovative Cultivation Program under grant CDUT2023BJCX008, and the State Key Laboratory of the Independent Research Project on Geological Disaster Prevention and Geological Environment Protection under grant SKLGP2021Z005.

Data Availability Statement: The data presented in this study are available on request from the corresponding author. The data are not publicly available due to their ongoing use in experimental research privacy restrictions.

Conflicts of Interest: The authors declare no conflicts of interest.

References

1. Wang, S.; Che, Y.; Xinggang, M. Integrated risk assessment of glacier lake outburst flood (GLOF) disaster over the Qinghai–Tibetan Plateau (QTP). *Landslides* **2020**, *17*, 2849–2863. [CrossRef]
2. Tang, M.; Xu, Q.; Wang, L.; Zhao, H.; Wu, G.; Zhou, J.; Li, G.; Cai, W.; Chen, X. Hidden dangers of ice avalanches and glacier lake outburst floods on the Tibetan Plateau: Identification, inventory, and distribution. *Landslides* **2023**, *20*, 2563–2581. [CrossRef]
3. Tang, M.; Li, G.; Zhao, H.; Wu, G.; Yang, W.; Guo, D. Advances in ice avalanches on the Tibetan Plateau. *J. Mt. Sci.* **2024**, *21*, 1814–1829. [CrossRef]
4. Kritikos, T.; Robinson, T.R.; Davies, T.R. Regional coseismic landslide hazard assessment without historical landslide inventories: A new approach. *J. Geophys. Res. Earth Surf.* **2015**, *120*, 711–729. [CrossRef]
5. Fan, X.; Yunus, A.P.; Yang, Y.H.; Subramanian, S.S.; Zou, C.; Dai, L.; Dou, X.; Narayana, A.C.; Avtar, R.; Xu, Q.; et al. Imminent threat of rock-ice avalanches in High Mountain Asia. *Sci. Total Environ.* **2022**, *836*, 155380. [CrossRef]

6. Liu, W.; Wang, M.; Song, B.; Yu, T.; Huang, X.; Jiang, Y.; Sun, Y. Surveys and chain structure study of potential hazards of ice avalanches based on optical remote sensing technology: A case study of southeast Tibet. *Remote Sens. Nat. Resour.* **2022**, *34*, 265–276. [CrossRef]
7. LaChapelle, E.R. Snow avalanches: A review of current research and applications. *J. Glaciol.* **1977**, *19*, 313–324. [CrossRef]
8. Kim, H.S.; Ji, Y. Three-dimensional geotechnical-layer mapping in Seoul using borehole database and deep neural network-based model. *Eng. Geol.* **2022**, *297*, 106489. [CrossRef]
9. Choubin, B.; Borji, M.; Mosavi, A.; Sajedi-Hosseini, F.; Singh, V.P.; Shamshirband, S. Snow avalanche hazard prediction using machine learning methods. *J. Hydrol.* **2019**, *577*, 123929. [CrossRef]
10. Choubin, B.; Borji, M.; Hosseini, F.S.; Mosavi, A.; Dineva, A.A. Mass wasting susceptibility assessment of snow avalanches using machine learning models. *Sci. Rep.* **2020**, *10*, 18363. [CrossRef]
11. Shi, J.J.; Zhang, W.; Wang, W.; Sun, Y.H.; Xu, C.Y.; Zhu, H.H.; Sun, Z.X. Randomly generating three-dimensional realistic schistous sand particles using deep learning: Variational autoencoder implementation. *Eng. Geol.* **2021**, *291*, 106235. [CrossRef]
12. Marjanović, M.; Kovačević, M.; Bajat, B.; Voženílek, V. Landslide susceptibility assessment using SVM machine learning algorithm. *Eng. Geol.* **2011**, *123*, 225–234. [CrossRef]
13. Kawabata, D.; Bandibas, J. Landslide susceptibility mapping using geological data, a DEM from ASTER images and an Artificial Neural Network (ANN). *Geomorphology* **2009**, *113*, 97–109. [CrossRef]
14. Sun, D.; Xu, J.; Wen, H.; Wang, D. Assessment of landslide susceptibility mapping based on Bayesian hyperparameter optimization: A comparison between logistic regression and random forest. *Eng. Geol.* **2021**, *281*, 105972. [CrossRef]
15. Lin, Z.; Ji, Y.; Sun, X. Landslide displacement prediction based on CEEMDAN method and CNN-BiLSTM model. *Sustainability* **2023**, *15*, 10071. [CrossRef]
16. Wang, H.; Zhang, L.; Yin, K.; Luo, H.; Li, J. Landslide identification using machine learning. *Geosci. Front.* **2021**, *12*, 351–364. [CrossRef]
17. Yao, J.; Wang, Y.; Wang, T.; Zhang, B.; Wu, Y.; Yao, X.; Zhao, Z.; Zhu, S. Assessing geological hazard susceptibility and impacts of climate factors in the eastern Himalayan syntaxis region. *Landslides* **2024**, *21*, 2195–2209. [CrossRef]
18. Tang, M.; Wang, L.; Liu, X. Distribution and risk of ice avalanche hazards in Tibetan Plateau. *Earth Sci.* **2022**, *47*, 4647–4662.
19. Tang, M.; Liu, X.; Li, G.; Zhao, H.; Xu, Q.; Zhu, X.; Li, W. Mechanism of ice avalanche in the Sedongpu sag, Yarlung Zangbo River basin-an experimental study. *Earth Sci. Front.* **2023**, *30*, 405. [CrossRef]
20. Zhao, B.; Su, L. Complex spatial and size distributions of landslides in the Yarlung Tsangpo River (YTR) basin. *J. Rock Mech. Geotech. Eng.* 2024, *in press*. [CrossRef]
21. Xia, Y. The Research of Distribution and Formation for Debris Flow Due to Break of Glacier Lake in the Ranwu-Peilong Section of the Sichuan-Tibet. Master's Thesis, Chongqing Jiaotong University, Chongqing, China, 2012.
22. Han, L.M. Geological Hazard Characteristics and Risk Assessment of Brahmaputra from Wolong to Zhibai Stream Segment. Master's Thesis, Chengdu University of Technology, Chengdu, China, 2018.
23. Zhang, W. Some Features of the Surge Glacier in the Mt. Namjagbarwa. *Mt. Res.* **1985**, *3*, 234–238.
24. Liu, J.; Cheng, Z. Meteorology Conditions for Frequent Debris Flows from Guxiang Valley in Tibet. *China Sci. Technol. Eng.* **2015**, *15*, 45–49.
25. Lü, R.R.; Tang, B.; Li, D. *Debris Flow and Environment in Tibet*; Chengdu University of Technology Press: Chengdu, China, 1999; pp. 106–136.
26. Liu, J.; Cheng, Z.; Li, Y.; Su, P. Characteristics of Glacier-Lake Breaks in Tibet. *J. Catastrophol.* **2008**, *23*, 57–62.
27. Guo, G.H.; Cheng, Z.L.; Wu, G.X.; Dang, C.; Liu, J.J. Risk Assessment of Glacial-lake Outburst Along the South Section of Sichuan-Tibet Highway. *Res. Soil Water Conserv.* **2009**, *16*, 50–55.
28. Lv, J.; Wang, Z.; Zhou, C. Discussion on the Occurrence of Yigong Landslide in Tibe. *Earth Sci.* **2003**, *28*, 107–110.
29. Liu, J.; Zhang, J.; Gao, B.; Li, Y.; Li, M.; Wujin, D.; Zhou, L. An overview of glacial lake outburst flood in Tibet. *China J. Glaciol. Geocryol.* **2019**, *41*, 1335–1347.
30. Qu, Y.; Xiao, J.; Pan, Y. Preliminary analysis on formation conditions of glacier debris flow in Southeast Tibet—A case of glacial debris flow in Tianmo Gully. *Water Resour. Hydropower Eng.* **2018**, *49*, 177–184. [CrossRef]
31. Liu, C.; Lv, J.; Tong, L.; Chen, H.; Liu, Q.; Xiao, R.; Tu, J. Research on glacial/rock fall-landslide-debris flows in Sedongpu basin along Yarlung Zangbo River in Tibet. *Geol. China* **2019**, *46*, 219–234. [CrossRef]
32. Wang, H.; Cui, P.; Li, Y.; Tang, J.; Wei, R.; Yang, A.; Zhou, L.; Bazai, N.A.; Zhang, G. Rock and ice avalanche-generated catastrophic debris flow at Chamoli, 7 February 2021: New insights from the geomorphic perspective. *Geomorphology* **2024**, *452*, 109110. [CrossRef]
33. Bondesan, A.; Francese, R.G. The climate-driven disaster of the Marmolada Glacier (Italy). *Geomorphology* **2023**, *431*, 108687. [CrossRef]
34. Mahboob, M.A.; Iqbal, J.; Atif, I. Modeling and simulation of glacier avalanche: A case study of gayari sector glaciers hazards assessment. *IEEE Trans. Geosci. Remote Sens.* **2015**, *11*, 5824–5834. [CrossRef]
35. Zhao, J.; Liang, S.; Li, X.; Duan, Y.; Liang, L. Detection of surface crevasses over Antarctic ice shelves using SAR imagery and deep learning method. *Remote Sens.* **2022**, *14*, 487. [CrossRef]
36. Berg, B.; Bassis, J. Crevasse advection increases glacier calving. *J. Glaciol.* **2022**, *68*, 977–986. [CrossRef]

37. He, K.; Zhang, X.; Ren, S.; Sun, J. Deep residual learning for image recognition. In Proceedings of the IEEE Conference on Computer Vision and Pattern Recognition, Las Vegas, NV, USA, 27–30 June 2016; pp. 770–778. [CrossRef]
38. He, K.; Zhang, X.; Ren, S.; Sun, J. Identity mappings in deep residual networks. In *Computer Vision–ECCV 2016, Proceedings of the 14th European Conference, Amsterdam, The Netherlands, 11–14 October 2016*; Proceedings, Part IV 14; Springer International Publishing: Berlin/Heidelberg, Germany, 2016; pp. 630–645. [CrossRef]
39. Hu, J.; Weng, B.; Huang, T.; Gao, J.; Ye, F.; You, L. Deep residual convolutional neural network combining dropout and transfer learning for ENSO forecasting. *Geophys. Res. Lett.* **2021**, *48*, e2021GL093531. [CrossRef]
40. Simonyan, K.; Zisserman, A. Very deep convolutional networks for large-scale image recognition. *arXiv* **2014**, arXiv:1409.1556. [CrossRef]
41. Pham, M.V.; Kim, Y.T. Debris flow detection and velocity estimation using deep convolutional neural network and image processing. *Landslides* **2022**, *19*, 2473–2488. [CrossRef]
42. Daubechies, I.; DeVore, R.; Foucart, S.; Hanin, B.; Petrova, G. Nonlinear approximation and (deep) ReLU networks. *Constr. Approx.* **2022**, *55*, 127–172. [CrossRef]
43. Garcia, J.A.; Waszek, L.; Tauzin, B.; Schmerr, N. Automatic identification of mantle seismic phases using a convolutional neural network. *Geophys. Res. Lett.* **2021**, *48*, e2020GL091658. [CrossRef]
44. Sharkawy, A.N. Principle of neural network and its main types. *J. Adv. App. Comput. Math.* **2020**, *7*, 8–19. [CrossRef]
45. Liu, Y.; Chen, X.; Yang, J.; Li, L.; Wang, T. Snow avalanche susceptibility mapping from tree-based machine learning approaches in ungauged or poorly-gauged regions. *Catena* **2023**, *224*, 106997. [CrossRef]
46. Li, H.; Xu, Q.; He, Y.; Fan, X.; Li, S. Modeling and predicting reservoir landslide displacement with deep belief network and EWMA control charts: A case study in Three Gorges Reservoir. *Landslides* **2020**, *17*, 693–707. [CrossRef]
47. Chi, J.; Kim, H.C. Prediction of arctic sea ice concentration using a fully data driven deep neural network. *Remote Sens.* **2017**, *9*, 1305. [CrossRef]
48. Shangxin, F.; Yufei, Z.; Yujie, W.; Shanyong, W.; Ruilang, C. A comprehensive approach to karst identification and groutability evaluation—A case study of the Dehou reservoir, SW China. *Eng. Geol.* **2020**, *269*, 105529. [CrossRef]
49. Sood, V.; Tiwari, R.K.; Singh, S.; Kaur, R.; Parida, B.R. Glacier boundary mapping using deep learning classification over Bara Shigri Glacier in Western Himalayas. *Sustainability* **2022**, *14*, 13485. [CrossRef]
50. Lin, G.F.; Chang, M.J.; Huang, Y.C.; Ho, J.Y. Assessment of susceptibility to rainfall-induced landslides using improved self-organizing linear output map, support vector machine, and logistic regression. *Eng. Geol.* **2017**, *224*, 62–74. [CrossRef]
51. Admassu, Y.; Hamdan, H.; Gautam, T. Multivariate statistical approach to re-evaluate the slake durability index test (ASTM 4644–08). *Eng. Geol.* **2016**, *209*, 12–20. [CrossRef]
52. Felicísimo, Á.M.; Cuartero, A.; Remondo, J.; Quirós, E. Mapping landslide susceptibility with logistic regression, multiple adaptive regression splines, classification and regression trees, and maximum entropy methods: A comparative study. *Landslides* **2013**, *10*, 175–189. [CrossRef]